The Effect of Planar Defects on the Optical Properties of Silver Nanostructures

Xue Ben, Penghui Cao, and Harold S. Park*

Department of Mechanical Engineering, Boston University, Boston, Massachusetts 02215, United States

ABSTRACT: We present a computational, atomistic electro-dynamics investigation of the effects of planar defects on the optical properties of silver nanocubes, where the planar defects we considered are different surface orientations, twins, partial dislocations, and full dislocations. We find that for nanocubes smaller than about 3 nm, the optical response is very sensitive to the specific surface structure resulting from the defects. However, the sensitivity, as measured by shifts in the plasmon resonance wavelength, is strongly reduced at larger sizes because of the decreasing importance of surface effects even when the majority of the atomic deformation due to the crystal defects is contained within the interior of the nanocube. Overall, this study suggests that the effects of individual crystalline defects on the optical properties of nanostructures can be safely ignored for nanostructure sizes larger than about 5 nm.
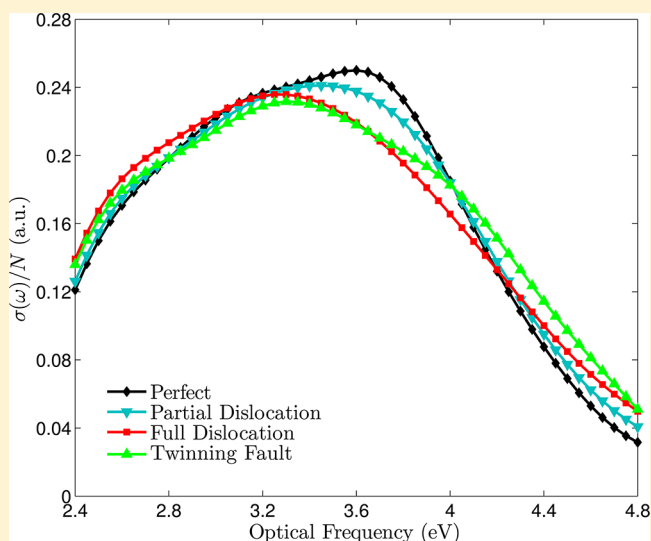
INTRODUCTION

The optical properties of small metal nanostructures have been investigated in great detail over the past two decades with most of the studies focusing on gold and silver nanostructures. Specifically, these two metals exhibit localized surface plasmon resonance (LSPR), which is a collective oscillation of the conduction electrons when excited by electromagnetic radiation within the visible spectrum.[1−3] Because of this, they have been utilized for a wide range of applications, including biosensing,[4] single molecule sensing and detection via surface-enhanced Raman scattering (SERS),[5−7] photothermal ablation treatments for cancer,[8,9] optical tagging and detection,[10,11] strain sensing,[12] metamaterials,[13] and many others.

In conjunction with these fascinating applications and experiments, computation has played a key role in elucidating the factors that control the LSPR wavelengths and optical properties of the nanostructures. For example, the discrete dipole approximation (DDA)[14] has been one of the most widely used computational techniques to study the optical properties of metal nanostructures.[3,15−20] Other popular approaches to calculating the optical properties of metal nanostructures include the finite difference time domain (FDTD) method,[21−23] volume integral methods,[24] and finite element methods.[25]

While these numerical methods have led to many seminal and important conclusions about the optical properties, there exist two main issues that preclude the application of existing numerical methods to the study of crystal defects on the optical properties. First, methods such as DDA and FDTD are both based on the bulk dielectric function, that is, the averaged atomic response of the material, and therefore do not resolve the optical properties at the atomic scale. Second, most numerical techniques work by discretizing a three-dimensional volume into a collection of small subdomains or volumes. Because of this, they are generally unable to explicitly represent the discrete atomic positions and, thus, the exact microstructure of a nanomaterial. For example, in the DDA, the volume is meshed into a set of discrete dipoles, which are constrained to sit on a regular, cubic grid. Because of this, the positions of the dipoles do not correspond to the actual positions occupied by atoms in an ideal face centered cubic (FCC) lattice. Taken one step further, one would experience considerable difficulty in applying these methods to study the optical properties of metal nanostructures that contain planar defects, and as a result, aside from a few studies[22,26] that considered pinhole-type defects in metal nanoshells, the effect of planar defects on the optical properties of metal nanostructures is largely unknown and unresolved.[27]

However, defects are common in metal nanostructures. For example, in solution-phase synthesized pentagonal nanowires or nanorods, the pentagonal nanowire also contains 5-fold twinned symmetry with the twins meeting in the center of the

nanowire.[28,29] Similarly, researchers have recently had success synthesizing small metal nanowires with diameters about 2 nm.[30,31] The mechanical properties of such small nanowires are known to be controlled by their extensive surface area;[32] however, it is not known how the discrete nature of different FCC surfaces, that is, {100} or {111}, impacts the resulting optical properties. Finally, many small metal nanoparticles are polycrystalline.[27] In all of these examples, the ability to resolve the effects of the defects on the optical properties depends crucially on having a computational method in which the discrete positions of all atoms are explicitly represented.

Therefore, we utilize the recently developed atomistic electrodynamic method of Jensen and Jensen[33,34] to perform a systematic study of planar defects on the optical properties of small silver nanostructures. This method is advantageous because it considers the actual discrete positions of atoms in the lattice regardless of whether the positions are ideal or correspond to those of a particular defect. Furthermore, this model is based on the careful parametrization of the atomic optical response. We consider three fundamental types of planar defects, that is, surfaces, twins, and intrinsic stacking faults, and in each case, we perform a comparison of the optical properties of the silver nanowire with the planar defect to a pristine one of the same size and number of atoms. In doing so, we are able to delineate the effects of each planar defect on the optical properties, and we find that surface effects dominate the optical response of nanocubes smaller than about 3 nm, while the effect of defects disappears for nanocubes larger than about 5 nm. The results are explained via simple analytical models of surface electron density and also via the relative polarizability of surface atoms as compared to those in the bulk.

ATOMISTIC ELECTRODYNAMIC METHOD

The atomistic electrodynamic model that we utilize in the present work to calculate the optical properties of small silver nanostructures was recently developed by Jensen and Jensen.[34,35] It is an extension of the capacitance-polarizability interaction model (CPIM),[35] which utilizes a point charge and dipole model to describe the interaction of the atoms with an external electric field. The point dipole-only model has been widely used in elucidating the optical properties of metal nanostructures most notably through the discrete dipole approximation (DDA).[3,14,17] However, as described in the Introduction, the DDA requires that the atoms lie on a periodic, cubic grid which does not match the FCC lattice structure of silver. In contrast, the atomistic electrodynamic method of Jensen and Jensen[34] calculates the optical properties directly from the actual position of atoms in the silver nanostructures. Furthermore, the method of Jensen and Jensen[34] directly describes the polarizability of each atom rather than considers the dielectric permittivity to be a bulk quantity, and thus, the optical properties obtained using this method are a direct outcome of the collective response of all atoms, whose individual optical response is described by fitted parameters from time-dependent density functional theory.[34]

We consider a silver cluster with N atoms where each atom is characterized by a frequency-dependent capacitance $c_i(\omega)$, described by a single Lorentzian oscillator, and a frequency-dependent polarizability $\alpha_{i,\alpha\beta}(\omega)$, described by two Lorentzian oscillators, that is,

$$c_i(w > 0) = c_{i,s}\left(\frac{w_{i,1}^2}{w_{i,1}^2 - w^2 - i\gamma_{i,1}w}\right) \quad (1)$$

$$
\begin{aligned}
\alpha_{i,\alpha\beta}(w > 0) &= \alpha_{i,s,\alpha\beta}\left(\frac{w_{i,1}^2}{w_{i,1}^2 - w^2 - i\gamma_{i,1}w}\right. \\
&\quad \left. + \frac{w_{i,2}(N)^2}{w_{i,2}(N)^2 - w^2 - i\gamma_{i,2}w}\right)
\end{aligned}
\quad (2)
$$

$$w_{i,2}(N) = w_{i,2}\left(1 + \frac{A}{N^{1/3}}\right) \quad (3)$$

where $c_{i,s} = 2.7529$ au is the static atomic capacitance, $\alpha_{i,s,\alpha\beta} = 49.9843$ au is the static atomic polarizability, $w_{i,1} = 0.0747$ au and $w_{i,2} = 0.0545$ au are the oscillator plasmon resonance frequencies, and $\gamma_{i,1} = 0.0604$ au and $\gamma_{i,2} = 0.0261$ au are the oscillator widths. Size-dependency of the optical properties is introduced through the size correction parameters $w_{i,2}(N)$ with $A = 2.7759$, which ensures that the absorption peak red shifts with increasing cluster size in agreement with experiments and also with time-dependent density functional theory (TDDFT) calculations. All of the parameters in eqs 1−3 were optimized by Jensen and Jensen[34] on the basis of TDDFT calculations for small silver nanostructures; we use the same parameters in the present work.

In the point dipole model, each atom has a frequency (ω)-dependent induced atomic charge $q_i^{ind}(\omega)$ and dipole $\mu_i^{ind}(\omega)$. Therefore, the total energy of the system is written as[34]

$$
\begin{aligned}
V &= \frac{1}{2}\sum_i^N \frac{q_i^{ind}(\omega)q_i^{ind}(\omega)}{c_i(\omega)} + \frac{1}{2}\sum_i^N \sum_{j\neq i}^N q_i^{ind}(\omega) \\
&\quad T_{ij}^{(0)}q_j^{ind}(\omega) - \sum_i^N \sum_{j\neq i}^N \mu_{i,\alpha}^{ind}(\omega)T_{ij,\alpha}^{(1)}q_j^{ind}(\omega) \\
&\quad + \frac{1}{2}\sum_i^N \mu_{i,\alpha}^{ind}(\omega)\alpha_{i,\alpha\beta}^{-1}(\omega)\mu_{i,\beta}^{ind}(\omega) \\
&\quad - \frac{1}{2}\sum_i^N \sum_{j\neq i}^N \mu_{i,\alpha}^{ind}(\omega)T_{ij,\alpha\beta}^{(2)}\mu_{j,\beta}^{ind}(\omega) \\
&\quad + \sum_i^N q_i^{ind}(\omega)\phi_i^{ext}(\omega) - \sum_i^N E_\alpha^{ext}(\omega)\mu_{i,\alpha}^{ind}(\omega) \\
&\quad - \lambda\left(q_{cluster} - \sum_i^N q_i^{ind}(\omega)\right)
\end{aligned}
\quad (4)
$$

where $T_{ij}^{(n)}$ are the interaction tensors of rank n, which are obtained using classical electrodynamics, where retardation effects are ignored in this work because of the small-size (<5 nm) nanostructures we consider in this work. $T_{ij}^{(0)}$, $T_{ij,\alpha}^{(1)}$, and $T_{ij,\alpha\beta}^{(2)}$ capture the charge−charge, charge−dipole, and dipole−dipole interactions, respectively. E^{ext} and ϕ_i^{ext} are the external electric field and potential, and λ is a Lagrange multiplier to ensure that the charge of the cluster remains constant. Furthermore, as originally formulated by Mayer[36] and as later utilized by Jensen and Jensen,[34] the interaction tensors are all normalized to eliminate the polarization catastrophe.

(a) Partial Dislocation   (b) Full Dislocation   (c) Twinning Fault
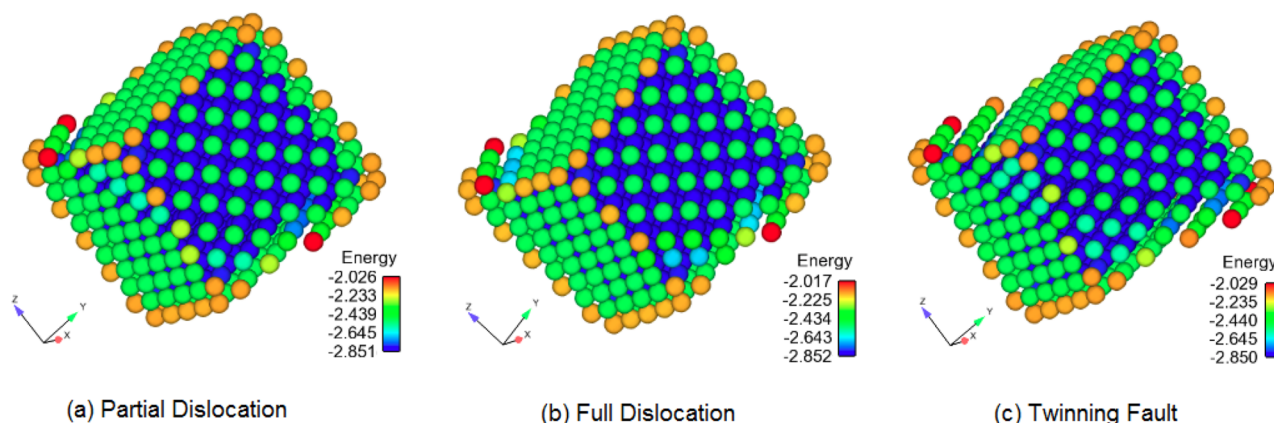
Figure 1. Energy-minimized configurations for $\langle 100 \rangle / \{100\}$ nanocube of size $2.0432 \times 2.0432 \times 2.0432$ nm^3 with a partial dislocation, full dislocation, and twinning fault. Atoms are colored by potential energy after energy minimization. Unit is in eV.

Minimizing the total energy V in eq 4 with respect to the induced atomic charges, dipoles, and Langrage multiplier λ leads to the following complex linear equations in matrix form

$$\begin{pmatrix} E^{ext}(\omega) \\ \phi^{ext}(\omega) \\ q^{cluster} \end{pmatrix} = \begin{pmatrix} A & -M & 0 \\ -M^T & -C & 1 \\ 0 & 1 & 0 \end{pmatrix} \begin{pmatrix} \mu^{ind}(\omega) \\ q^{ind}(\omega) \\ \lambda \end{pmatrix} \quad (5)$$

The interaction matrix on the right-hand side of eq 5 is a full matrix comprised of A, M, and C, where the elements are defined using the interaction tensors T_{ij}^n, that is,

$$A_{ij,\alpha\beta} = -T_{ij,\alpha\beta}^{(2)}(i \neq j); \quad A_{ii,\alpha\beta} = \alpha_{i,\alpha\beta}(\omega)^{-1} \quad (6)$$

$$C_{ij} = T_{ij,\alpha}^{(0)}(i \neq j); \quad C_{ii} = c_i(\omega)^{-1} \quad (7)$$

$$M_{ij,\alpha} = T_{ij,\alpha}^{(1)}(i \neq j); \quad M_{ii,\alpha} = 0 \quad (8)$$

Inverting the full interaction matrix on the right-hand side of eq 5 will lead to the solution of induced dipole moments and charges for each atom, that is,

$$\begin{pmatrix} \mu^{ind}(\omega) \\ q^{ind}(\omega) \\ \lambda \end{pmatrix} = \begin{pmatrix} A & -M & 0 \\ -M^T & -C & 1 \\ 0 & 1 & 0 \end{pmatrix}^{-1} \begin{pmatrix} E^{ext}(\omega) \\ \phi^{ext}(\omega) \\ q^{cluster} \end{pmatrix}$$

$$= \begin{pmatrix} B & g & h_1 \\ g^T & D & h_2 \\ h_1^T & h_2^T & h_3 \end{pmatrix} \begin{pmatrix} E^{ext}(\omega) \\ \phi^{ext}(\omega) \\ q^{cluster} \end{pmatrix} \quad (10)$$

All of the structural and geometric information for the given nanostructure under consideration is contained in this $(4N + 1)$ by $(4N + 1)$ matrix in eq 5, which captures both the atom type as well as the influence of the actual atomic positions and thus enables us to study the effects of surfaces and other crystalline defects (dislocations, twins) on the resulting optical properties.

The frequency-dependent molecular polarizability can then be quantified in terms of the inverted interaction matrix as

$$\alpha_{\alpha\beta}^{mol}(\omega) = \sum_{i,j}^{N} (B_{ij,\alpha\beta}(\omega) - r_{i,\alpha}D_{ij}(\omega)r_{j,\beta}) \quad (11)$$

where the imaginary parts of eq 11 directly relate to the absorption spectra of the metal cluster as

$$\sigma(\omega) = \frac{4\pi\omega}{c} \text{Im}[\alpha(\omega)] \quad (12)$$

In all of the numerical examples below, we report the absorption calculated as the average of the three principal cross sections.

NUMERICAL RESULTS

Simulation Details. Having described the computational approach we used to calculate the optical properties, we now describe the silver nanostructures we studied in the present work. Specifically, we studied silver nanocubes with the majority of the studies performed on those having a $\langle 100 \rangle$ axial orientation with $\{100\}$ surfaces, which we refer to as a $\langle 100 \rangle / \{100\}$ nanocube. We focus our results on these nanocubes with 2 nm cross-sectional length though we considered nanocubes of up to 5 nm cross-sectional length to study how surfaces, dislocations, and twins impact the optical properties of larger silver nanostructures. The nanocubes were created assuming ideal atomic positions, that is, with silver atoms lying in an FCC unit cell with the lattice constant of silver being $a = 4.09$ Å.

To study surface effects, we considered a nanocube with the same $\langle 100 \rangle$ axial orientation but rotated 45 degrees about the axial axis in order to generate $\{110\}$ and not $\{100\}$ surfaces as illustrated in Figure 2b. This nanocube thus contains four $\{110\}$ surfaces and two $\{100\}$ surfaces. We will refer to this nanocube as a $\langle 100 \rangle / \{110\}$ nanocube.

We considered three types of defects aside from surfaces: full dislocations, partial dislocations, and twins all created in the $\langle 100 \rangle$ nanocube with $\{100\}$ surfaces as illustrated in Figure 1. Full dislocations were generated by dividing the atoms in the cube into two groups by the center $\{111\}$ plane and then by shearing one group of atoms with respect to the other by the standard full dislocation displacement of $((a/2)[10\bar{1}])$, where $a = 4.09$ Å is the lattice constant for silver. For the partial dislocation, the same procedure was applied except with a different displacement of $((a/6)[11\bar{2}])$. The twin fault was generated by first creating a single partial dislocation according to the procedure just described and then by shearing an adjacent $\{111\}$ plane by the same amount to generate a twin fault.
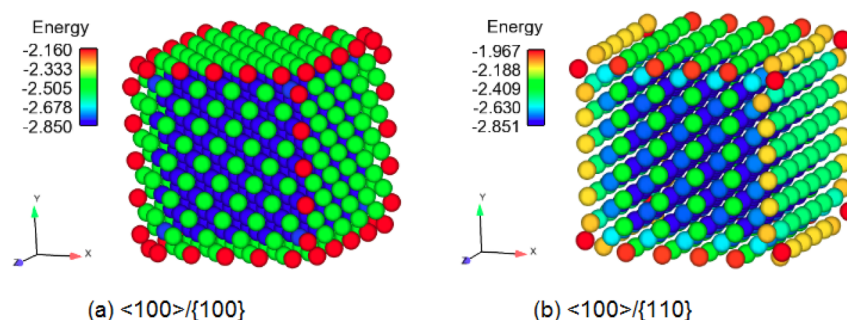
Figure 2. Equilibrium atomic positions for (a) $\langle 100 \rangle/\{100\}$ nanocube with size $2.0432 \times 2.0432 \times 2.0432$ nm^3 and (b) $\langle 100 \rangle/\{110\}$ nanocube with size $2.2000 \times 2.0363 \times 2.0363$ nm^3 after energy minimization. Atoms are colored by potential energy. Unit is in eV.

For all of the above-mentioned structures (i.e., perfect $\langle 100 \rangle/\{100\}$ nanocube, $\langle 100 \rangle/\{110\}$ nanocube, and $\langle 100 \rangle/\{100\}$ nanocube with dislocations and twins), we then took the resulting atomic positions and determined the minimum energy configuration via conjugate gradient energy minimization of each structure using the open-source simulation code LAMMPS[37] using a realistic embedded atom method (EAM) potential[38] to model the interactions of the silver atoms. A comparison between the $\langle 100 \rangle/\{100\}$ and $\langle 100 \rangle/\{110\}$ nanocubes after energy minimization is given in Figure 2, while the $\langle 100 \rangle/\{100\}$ nanocube with partial dislocation, full dislocation, and twin is shown later. Typically, the energy minimization results in a small contraction of the cube, which is consistent with previous atomistic simulations of FCC metal nanostructures which found that surface atoms tend to contract toward the bulk in order to increase their electron density.[39]

The atomistic electrodynamic method was then run using the resulting energy minimized atomic positions to calculate the optical properties. Using these positions, we can generate the full interaction matrix needed to calculate the dipoles and charges in eq 9, which are then used to extract information about the absorption cross section via eq 12 for each cluster. Because some of the structures, particularly those in which the nanocube is rotated to generate the $\{110\}$ transverse surfaces, have a slightly different number of atoms, we have for consistency normalized all results for the absorption cross section by the total number of atoms in each structure. Table 1

Table 1. Dimensions of $\langle 100 \rangle$ Nanocubes with $\{100\}$ Surfaces with Total Number of Atoms N_{Atoms} for Each Nanocube and the Total Number of Atoms $N_{dislocation}$ Shifted by the Introduction of a Dislocation (Full, Partial, Twin)

nanocube	size	N_{Atoms}	$N_{dislocation}$
$\langle 100 \rangle/\{100\}$	$2.0432 \times 2.0432 \times 2.0432$ nm^3	665	378

shows the size, number of atoms, and number of atoms for the $\langle 100 \rangle/\{100\}$ nanocube shifted because of the three crystal defects (full and partial dislocations, twin). We emphasize that for the larger nanocubes we considered, the same proportion of atoms were shifted in order to enable a consistent size effect comparison.

The nanocube geometry was chosen for two main reasons. First, in the atomistic electrodynamic model for silver developed by Jensen and Jensen,[34] the model was parametrized to be valid for incident energy values between about 2.4 and 4.8 eV. This range of incident energy values limits the potential geometry that can be studied to those that are more cubic as larger aspect ratio geometries such as one-dimensional

nanowires would exhibit plasmon resonances at lower energies outside the valid energy range for the atomistic electrodynamic model because of the red shift that occurs with increasing aspect ratio. Second, the cubic geometry enables us to delineate the most important driving forces for the evolution of the plasmonic response when different surface orientations and crystal defects are introduced into the system. We expect that the key findings below will hold for other, more complex nanostructure geometries though the specific length scales at which the transition from surface-dominated to bulk-dominated plasmonic response may vary slightly depending on the specific geometry that is considered.

Simulation Results. *Surfaces.* We first discuss the effects of changing the surfaces of the $\langle 100 \rangle$ nanocube from $\{100\}$ to $\{110\}$, where the results for 2 nm nanocubes are shown in Figure 3. Nanocubes of similar cubic size were considered in
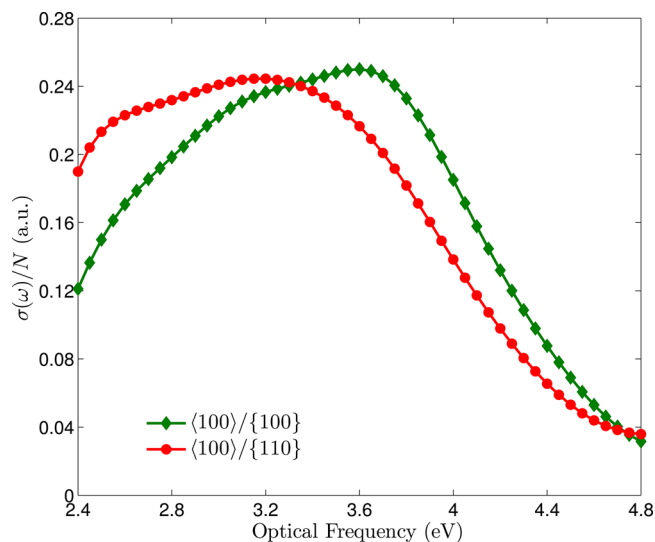
Figure 3. The absorption cross sections of $2.0432 \times 2.0432 \times 2.0432$ nm^3 $\langle 100 \rangle/\{100\}$ and $2.2000 \times 2.0363 \times 2.0363$ nm^3 $\langle 100 \rangle/\{110\}$ nanocubes. Values are averaged over the total number of atoms for each nanocube.

order to ensure that the optical response we report can be attributed to the differences in discrete surface structure of the nanocubes.

As shown from the averaged optical response spectrum in Figure 3, the LSPR is very sensitive to the discrete atomic structure of the nanocube. The two nanocubes exhibit very different resonance behavior, LSPR position, and absorption widths. Specifically, the LSPR frequency for the $\langle 100 \rangle/\{100\}$
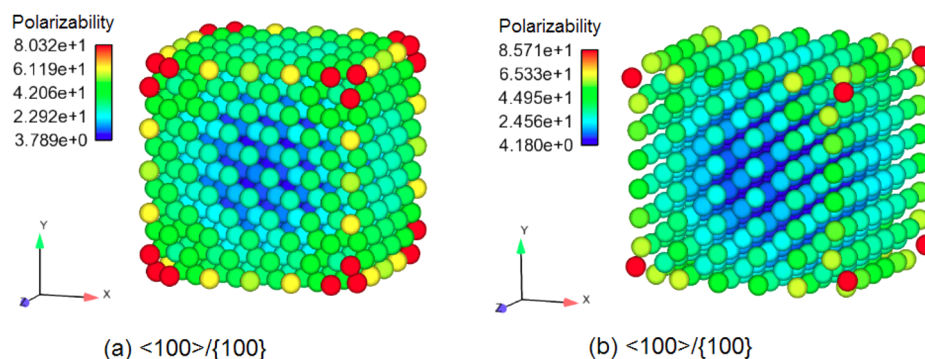
Figure 4. The effective polarizability distribution for $\langle 100\rangle/\{100\}$ and $\langle 100\rangle/\{110\}$ nanocubes with similar size, i.e., $2.0432 \times 2.0432 \times 2.0432$ nm³ for the $\langle 100\rangle/\{100\}$ nanocube and $2.2000 \times 2.0363 \times 2.0363$ nm³ for the $\langle 100\rangle/\{110\}$ nanocube. Unit is in au.

nanocube is 0.4 eV higher than the $\langle 100\rangle/\{110\}$ nanocube (3.6 and 3.2 eV, respectively), corresponding to a 43 nm red shift, even though they are nanocubes of the same shape and size.

Before conducting a more rigorous analysis, it is instructive to first compare the mechanical potential energy of the nanocubes in Figure 2 with the corresponding polarization distribution in Figure 4. From the minimized energy configurations seen in Figure 2, it is clear that the corner, surface, and edge atoms have a higher potential energy as compared to the bulk atoms for both the $\langle 100\rangle/\{110\}$ and the $\langle 100\rangle/\{100\}$ nanocubes because of their relative under-coordination as compared to bulk atoms, where bulk refers to those atoms in the interior of the nanocube. Similarly, atoms at the edges, surfaces, and corners in Figure 4 also have higher polarizabilities than the atoms within the bulk. Therefore, we expect that it is the surface effects for these small nanocubes that control the polarizability distribution. Furthermore, because the individual atomic polarizabilities determine the nanocluster polarizability and therefore the optical response of the nanocube, we can expect that it is surface effects that lead to the large difference in the optical response of the nanocubes as shown in Figure 3.

We can gain more insights into the effects of surfaces on the LSPR by comparing the free-electron density at the surfaces for the two nanoclusters because the LSPR arises from the resonant oscillations of electrons in response to an external electromagnetic field. The incident field shifts the negative charges collectively with respect to the positive ionic back-ground resulting in net negative and positive charges at the opposite side of the particle.[40] It is this attraction of the alternating charges that forms the restoring force, controls the eigenfrequency of the oscillation, and thus determines the LSPR frequency. Because the attraction mainly comes from the net surface electrons, the restoring force is proportional to the surface electron density, and the eigenfrequency should be proportional to the square root of the surface electron density n^{surf}.

We now perform a simple analysis on the basis of the surface structures of the two nanocubes. Here, we only consider the contribution from the outermost layer of surface for simplicity, which is shown to result in very good accuracy. For the $\langle 100\rangle/\{100\}$ nanocube, the surface electron densities are the same for each of the six $\{100\}$ surfaces, and each atom contributes one free electron, and so the surface electron density is simply the number of surface atoms divided by the surface area (i.e., the surface atomic density). Assuming that the atoms at the center of each surface belong to that surface, while the atoms at the

edges are shared by two surfaces and while the atoms at the corners are shared by four surfaces, the number of surface atoms is $N_{\mathrm{surf}} = N_{\mathrm{center}} + N_{\mathrm{edge}}/2 + N_{\mathrm{corner}}/4$, then the average surface electron density is $n^{\mathrm{surf}} = 1/3\{[N_{xy}/(d_x \times d_y)] + [N_{yz}/(d_y \times d_z)] + [N_{zx}/(d_z \times d_x)]\}$. Details of the decomposition of surface atoms into center, bulk, and corner are given for the $\{100\}$ and $\{110\}$ surfaces in Table 2 and Table 3, respectively.

Table 2. Decomposition of Surface Atoms into Center, Edge, and Corner for the $\{100\}$ Surface of a $\langle 100\rangle/\{100\}$ Nanocube

	$\langle 100\rangle/\{100\}$ nanocube			
surface	N_{center}	N_{edge}	N_{corner}	area (nm²)
$\{100\}$	40	20	0	2.0432×2.0432

Table 3. Decomposition of Surface Atoms into Center, Edge, and Corner for the $\{110\}$ and $\{100\}$ Surfaces of a $\langle 100\rangle/\{110\}$ Nanocube

	$\langle 100\rangle/\{110\}$ nanocube			
surface	N_{center}	N_{edge}	N_{corner}	area (nm²)
$\{100\}$	36	24	4	2.0363×2.0363
$\{110\}$	24	20	4	2.2000×2.0363

For the $\langle 100\rangle/\{100\}$ nanocube, the surface electron density is, following Table 2, $n_1^{\mathrm{surf}} = (40 + 20/2)/(2.0432 \times 2.0432) = 11.9770$ nm⁻². For the $\langle 100\rangle/\{110\}$ nanocube, there are two identical $\{100\}$ and four identical $\{110\}$ surfaces, which then following Table 3 leads to a surface electron density of $n_2^{\mathrm{surf}} = (1/3)[(36 + 24/2 + 4/4)/(2.0363 \times 2.0363) + 2 \times (24 + 20/2 + 4/4)/(2.0363 \times 2.2000)] = 9.1474$ nm⁻². Because the LSPR frequency is proportional to the eigenfrequency of this oscillating spring induced by the restoring force, $\omega_{\mathrm{res}} \propto (n^{\mathrm{surf}})^{1/2}$, we will have $(\omega_1/\omega_2) = (n_1/n_2)^{1/2} = (11.9770/9.1474)^{1/2} = 1.1442$ in good agreement with our atomistic electrodynamic simulation results where $(\omega_1/\omega_2) = (3.6\ \mathrm{eV}/3.2\ \mathrm{eV}) = 1.1250$. This again verifies that the different optical responses of the $\langle 100\rangle/\{100\}$ and $\langle 100\rangle/\{110\}$ nanocubes with similar size are indeed controlled by their different surfaces.

Our results agree with those of Jensen and Jensen,[33] who found that for nanoclusters with less than around 700 atoms, most atoms have surfacelike polarizabilities which further justifies our analysis of the surface electron density differences for the 2 nm nanocubes. However, this also suggests that because the nanocluster polarizability can be distinguished into

distinctive bulk and surface components at larger sizes,[33] we should expect the importance of the surface effects to decrease at larger sizes; we will discuss this in further detail in a later section.

Partial Dislocations, Full Dislocations, and Twins. We next analyze the optical properties of 2 nm cross-sectional length $\langle 100 \rangle/\{100\}$ silver nanocubes containing either a single partial dislocation, full dislocation, or twin fault; a comparison of the optical absorption for all three defect cases with a perfect $\langle 100 \rangle/\{100\}$ silver nanocube without any such defects is given in Figure 5.
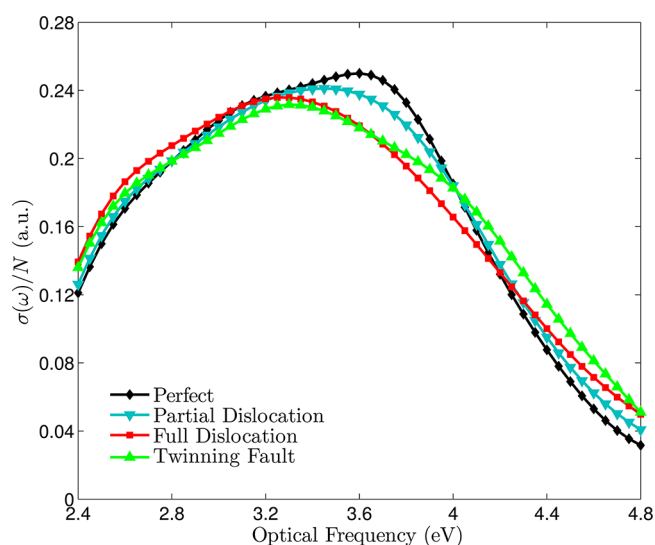
Figure 5. The absorption spectrum of $\langle 100 \rangle\{100\}$ nanocube of size $2.0432 \times 2.0432 \times 2.0432$ nm³ for perfect nanocube (black), partial dislocation (blue), full dislocation (red), and twin (green).

There are several common characteristics to note. First, as the severity of the defect increases (i.e., from defect-free nanocube to those containing a partial dislocation, full dislocation, and twin fault), the absorption maximum decreases gradually. Second, the defects result in a red shift of the LSPR frequency, where a summary of the resulting LSPR wavelength for all defects in the $\langle 100 \rangle/\{100\}$ nanocubes we considered is given in Table 4. There, it is seen that the LSPR red shift due to

Table 4. LSPR Frequency, Wavelength, and Width for $2.0432 \times 2.0432 \times 2.0432$ nm3 $\langle 100 \rangle/\{100\}$ Nanocube with and without Defects

LSPR frequencies for $\langle 100 \rangle/\{100\}$ nanocube				
$\langle 100 \rangle/\{100\}$	perfect	partial	full	twins
LSPR frequency	3.6 eV	3.45 eV	3.3 eV	3.3 eV
LSPR wavelength	344 nm	359 nm	375 nm	375 nm
plasmon width	2.04 eV	2.15 eV	2.29 eV	2.39 eV

a single full dislocation and twin boundary is 31 nm, almost exactly double that of the 15 nm shift caused by a partial dislocation.

It is also of interest to compare the plasmon width (i.e., the full width at half-maximum) in Figure 5 of the optical response for the same structure containing different defects. For the defect-free $\langle 100 \rangle/\{100\}$ nanocube, the damping mechanism is primarily due to the scattering of electrons at the nanocube surfaces. However, when introducing a partial dislocation to the

nanocube, there is an additional damping effect caused by the scattering of electrons at the planar defect because of the changes in atomic bond length across the dislocation. Furthermore, there are additional surface steps and corners because of the partial dislocation which further broaden the optical spectrum. Additional broadening is observed for the full dislocation and the twin fault because of the increased damping effects as summarized in Table 4, which demonstrates that the atomistic electrodynamic model can effectively capture the internal damping and surface scattering caused by scattering of electrons on defects and also on surface boundaries and surface steps.[41]

To further quantify the dominant effect of surfaces on the variation in optical properties seen in Figure 5, we consider the effective atomic polarizability for each atom, which is dependent on its position in the nanocube, as shown in Figure 6. We find that all atoms within the bulk of the nanocube behave as bulk atoms (using the definition in Jensen and Jensen[33] that the ratio of the effective polarizability to the bulk polarizability is less than 0.5) with no distinction between those atoms sitting immediately around the defect (full dislocation, partial dislocation, twin fault) and the other bulk atoms, where the number of bulk and surface atoms via the polarizability criterion has been summarized in Table 5 for the perfect nanocube as well as for all cases with defects. Specifically, Table 5 shows that the number of surface atoms (as delineated by polarizability) increases as the defect severity increases, which makes sense because of the additional surface steps and edges introduced by the dislocations and twin faults. It is these additional surface atoms that result in the LSPR shifts and the broadening of the resonance.

Size Effects. So far, our discussion has centered on the effects of defects for a single size. The question remains as to how the various defects (surfaces, dislocations) impact the optical properties at larger sizes. We address that question here.

We conducted a size-effect study by calculating the absorption for the $\langle 100 \rangle/\{100\}$ nanocubes with and without a single partial dislocation, full dislocation, and twin for cross-sectional sizes up to 5.3 nm while also considering $\langle 100 \rangle/\{110\}$ nanocubes without any defects for cross-sectional sizes up to 5.3 nm. For the $\langle 100 \rangle/\{100\}$ nanocube without defects, we found that the absorption maximum occurred at 3.6 and 3.24 eV for nanocubes with 2 and 4 nm cross-sectional lengths, respectively. We compare the red shift with the recent experimental results on silver nanospheres by Scholl et al.,[42] who developed an analytical quantum theory of particle permittivity within Mie theory and who found absorption peaks at 3.8 and 3.5 eV for silver nanospheres with diameters of 2 and 4 nm, respectively. Accounting for the difference in geometry between the nanocubes in the present work and the nanospheres that were studied experimentally and theoretically, we find that the present computational model is able to qualitatively capture the size-dependent LSPR frequency evolution.

From our previous discussion on the effective polarizability distribution for $\langle 100 \rangle/\{100\}$ and $\langle 100 \rangle/\{110\}$ nanocubes, we established that for 2 nm nanocubes, the surface atom polarizabilities dominated the bulk atom polarizabilities in controlling the optical absorption. However, we have not established the size at which the bulk atoms will begin to control the optical properties. To do so, we perform a size-dependent study on the surface electron density and bulk electron density (total free electrons divided by the volume of
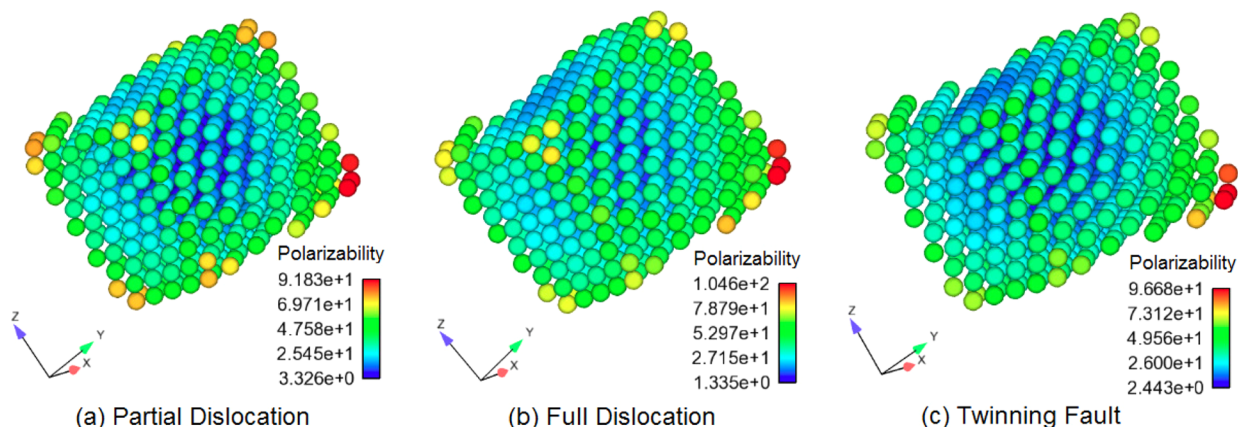
Figure 6. The effective polarizability distribution for ⟨100⟩/{100} nanocube of size 2.0432 × 2.0432 × 2.0432 nm³ with partial dislocation, full dislocation, and twinning fault. Unit is in au.

Table 5. Decomposition of Atoms into Bulk and Surface via Polarizability Criteria of Jensen and Jensen,[33] where the Average Effective Bulk (α_{bulk}) and Surface (α_{surf}) Polarizability Are Shown for Each Structure

	surface and bulk atom polarizability			
⟨100⟩/{100}	N_{bulk}	α_{bulk} (au)	N_{surf}	α_{surf}(au)
perfect	141	75.72	524	242.60
partial	126	71.60	539	231.87
full	119	69.78	546	227.96
twin	114	68.23	551	228.03

the nanocube) changes because the LSPR resonance is essentially the collective resonance oscillation of the free electrons, and the LSPR frequency is proportional to the plasmon frequency $\omega_{sp} = [(ne)^2/(m\varepsilon_0)]^{1/2}$,[43,44] where n is the bulk free electron density.

Specifically, we compute the ratio of LSPR frequency (ω_1/ω_2), square root of surface electron density ratio, and square root of bulk electron density ratio for ⟨100⟩/{100} and ⟨100⟩/{110} nanocubes. As seen in Figure 7, the LSPR frequency ratio for ⟨100⟩/{100} to ⟨100⟩/{110} follows the same trend
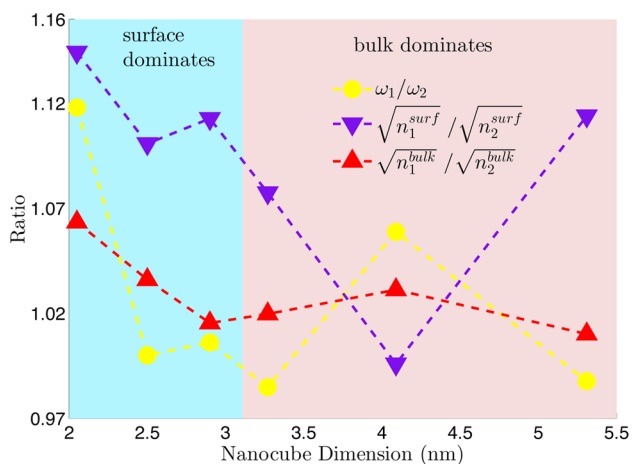
Figure 7. The ratio of LSPR frequency (yellow circles), square root of surface electron density (purple triangles), and square root of volume electron density (red triangles). The ratio in each case is calculated as that of the ⟨100⟩/{100} value (structure 1) to the ⟨100⟩/{110} (structure 2) value for each size.

as the surface electron density ratio $(n_1^{surf})^{1/2}/(n_2^{surf})^{1/2}$ for nanocube sizes smaller than about 3.3 nm. However, for larger sizes, the LSPR frequency ratio ω_1/ω_2 tends to follow the bulk electron density ratio $(n_1^{bulk})^{1/2}/(n_2^{bulk})^{1/2}$, while for the same size range greater than 3 nm, $(n_1^{bulk})^{1/2}/(n_2^{bulk})^{1/2}$ approaches a value of about 1.01. Therefore, this implies that for nanocube sizes smaller than about 3 nm, the surface electron density dominates, while for larger sizes the bulk electron density dominates. The ratios of surface electron density and bulk density are not identical to ω_1/ω_2 because both should be modulated by quantum effects. Additionally, the jump in surface electron density ratio from 4 to 5 nm nanocube dimension occurs because the ⟨100⟩/{110} nanocubes are in fact not perfect nanocubes in that they have different side lengths resulting from the fact that they have two {100} and four {110} surfaces, which results in a variation in the total number of electrons at the surfaces.

Having established that the discrete surface effects become less important for nanocube sizes larger than about 3 nm, we perform the same size effect study for the crystal defects, that is, full dislocation, partial dislocation, and twin fault. Interestingly, we find the same trend, that is, that for nanocubes larger than about 3 nm, the optical absorption spectrum for a ⟨100⟩/{100} nanocube with a single partial or full dislocation or twin fault is essentially identical as shown for a 5.3 nm nanocube in Figure 8. The rationale is similar to the surface case: because we previously established that it was the surface steps caused by the crystal defects that were the cause for the large LSPR frequency red shift for the 2 nm size, it is intuitively clear that for larger sizes, as the surface effects diminish, the effect of crystal defects on the optical properties of nanocubes would also diminish at larger nanocube sizes.

Overall, these results imply that experimentalists can essentially ignore the discrete atomic structure resulting from defects for nanostructures with characteristic sizes larger than about 5 nm. Furthermore, the variations in optical properties for larger size nanostructures may not be attributed to individual crystal defects such as surfaces or dislocations and are likely due to other effects, such as retardation (dynamic depolarization, radiative damping)[45,46] and nonlocal effects.[47−49]
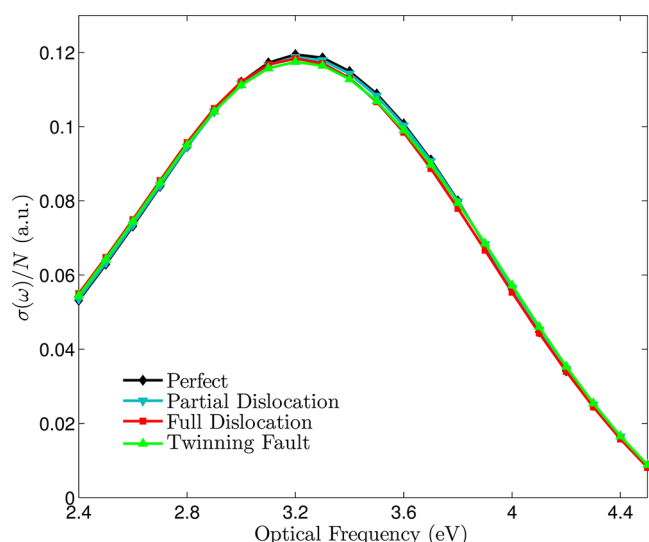
Figure 8. The absorption cross section of ⟨100⟩/{100} nanocube of size $5.3 \times 5.3 \times 5.3$ nm³ for defect-free case (black), partial dislocation (blue), full dislocation (red), and twin fault (green).

CONCLUSION

We have utilized a computational atomistic electrodynamics model to investigate the effects of various crystalline defects (surfaces, partial dislocations, full dislocations, twins) on the optical properties of small silver nanocubes. While the crystal defects can have a substantial effect for nanocubes smaller than about 3 nm because of the dominance of surface effects at those sizes, the effects are mitigated for larger nanocubes.

AUTHOR INFORMATION

Corresponding Author
*E-mail: parkhs@bu.edu.

Notes
The authors declare no competing financial interest.

REFERENCES

(1) Ozbay, E. Plasmonics: Merging Photonics and Electronics at Nanoscale Dimensions. *Science* **2006**, *311*, 189−193.
(2) Barnes, W. L.; Dereux, A.; Ebbeson, T. W. Surface Plasmon Subwavelength Optics. *Nature* **2003**, *424*, 824−830.
(3) Kelly, K. L.; Coronado, E.; Zhao, L. L.; Schatz, G. C. The Optical Properties of Metal Nanoparticles: the Influence of Size, Shape, and Dielectric Environment. *J. Phys. Chem. B* **2003**, *107*, 668−677.
(4) Anker, J. N.; Hall, W. P.; Lyandres, O.; Shah, N. C.; Zhao, J.; Duyne, R. P. V. Biosensing with Plasmonic Nanosensors. *Nat. Mater.* **2008**, *7*, 442−453.
(5) Kneipp, K.; Moskovits, M.; Kneipp, H. E. *Surface-Enhanced Raman Scattering*; Springer: Berlin, 2006.
(6) Kneipp, K.; Wang, Y.; Kneipp, H.; Perelman, L. T.; Itzkan, I.; Dasari, R. R.; Feld, M. S. Single Molecule Detection Using Surface-Enhanced Raman Scattering. *Phys. Rev. Lett.* **1997**, *78*, 1667−1670.
(7) Nie, S.; Emory, S. R. Probing Single Molecules and Single Nanoparticles by Surface-Enhanced Raman Scattering. *Science* **1997**, *275*, 1102−1106.
(8) Hirsch, L. R.; Gobin, A. M.; Lowery, A. R.; Tam, F.; Drezek, R. A.; Halas, N. J.; West, J. L. Metal Nanoshells. *Annu. Biomed. Eng.* **2006**, *34*, 15−22.

(9) Huang, X.; El-Sayed, I. H.; Qian, W.; El-Sayed, M. A. Cancer Cell Imaging and Photothermal Therapy in the Near-Infrared Region by Using Gold Nanorods. *J. Am. Chem. Soc.* **2006**, *128*, 2115−2120.
(10) Nicewarner-Pena, S. R.; Freeman, R. G.; Reiss, B. D.; He, L.; Pena, D. J.; Walton, I. D.; Cromer, R.; Keating, C. D.; Natan, M. J. Submicrometer Metallic Barcodes. *Science* **2001**, *294*, 137−141.
(11) Mock, J. J.; Oldenburg, S. J.; Smith, D. R.; Schultz, D. A.; Schultz, S. Composite Plasmon Resonant Nanowires. *Nano Lett.* **2002**, *2*, 465−469.
(12) Stone, J. W.; Sisco, P. N.; Goldsmith, E. C.; Baxter, S. C.; Murphy, C. J. Using Gold Nanorods to Probe Cell-Induced Collagen Deformation. *Nano Lett.* **2007**, *7*, 116−119.
(13) Biener, J.; Nyce, G. W.; Hodge, A. M.; Biener, M. M.; Hamz, A. V.; Maier, S. A. Nanoporous Plasmonic Metamaterials. *Adv. Mater.* **2008**, *20*, 1211−1217.
(14) Draine, B. T.; Flatau, P. J. Discrete-Dipole Approximation for Scattering Calculations. *J. Opt. Soc. Am. A* **1994**, *11*, 1491−1499.
(15) Brioude, A.; Jiang, X. C.; Pileni, M. P. Optical Properties of Gold Nanorods: DDA Simulations Supported by Experiments. *J. Phys. Chem. B* **2005**, *109*, 13138−13142.
(16) Jain, P. K.; Huang, W.; El-Sayed, M. A. On the Universal Scaling Behavior of the Distance Decay of Plasmon Coupling in Metal Nanoparticle Pairs: A Plasmon Ruler Equation. *Nano Lett.* **2007**, *7*, 2080−2088.
(17) Jain, P. K.; Lee, K. S.; El-Sayed, I. H.; El-Sayed, M. A. Calculated Absorption and Scattering Properties of Gold Nanoparticles of Different Size, Shape, and Composition: Applications in Biological Imaging and Biomedicine. *J. Phys. Chem. B* **2006**, *110*, 7238−7248.
(18) Hao, E.; Schatz, G. C. Electromagnetic Fields Around Silver Nanoparticles and Dimers. *J. Chem. Phys.* **2004**, *120*, 357−366.
(19) Lee, K.-S.; El-Sayed, M. A. Gold and Silver Nanoparticles in Sensing and Imaging: Sensitivity of Plasmon Response to Size, Shape, and Metal Composition. *J. Phys. Chem. B* **2006**, *110*, 19220−19225.
(20) Myroshnychenko, V.; Rodriguez-Fernandez, J.; Pastoriza-Santos, I.; Funston, A. M.; Novo, C.; Mulvaney, P.; Liz-Marzan, L. M.; de Abajo, F. J. G. Modelling the Optical Response of Gold Nanoparticles. *Chem. Soc. Rev.* **2008**, *37*, 1792−1805.
(21) Yee, K. S. Numerical Solution of Initial Boundary Value Problems Involving Maxwell's Equations in Isotropic Media. *IEEE Trans. Antennas Propag.* **1966**, *14*, 302−307.
(22) Oubre, C.; Nordlander, P. Optical Properties of Metallodielectric Nanostructures Calculated Using the Finite Difference Time Domain Method. *J. Phys. Chem. B* **2004**, *108*, 17704−17747.
(23) McMahon, J. M.; Gray, S. K.; Schatz, G. C. Nonlocal Optical Response of Metal Nanostructures with Arbitrary Shape. *Phys. Rev. Lett.* **2009**, *103*, 097403.
(24) Kottmann, J. P.; Martin, O. J. F. Accurate Solution of the Volume Integral Equation for High-Permittivity Scatterers. *IEEE Trans. Antennas Propag.* **2000**, *48*, 1719−1726.
(25) Volakis, J. L.; Chatterjee, A.; Kempel, L. C. Review of the Finite-Element Method for Three-Dimensional Electromagnetic Scattering. *J. Opt. Soc. Am. A* **1994**, *11*, 1422−1433.
(26) Hao, E.; Li, S.; Bailey, R. C.; Zou, S.; Schatz, G. C.; Hupp, J. T. Optical Properties of Metal Nanoshells. *J. Phys. Chem. B* **2004**, *108*, 1224−1229.
(27) Goubet, N.; Yan, C.; Polli, D.; Portales, H.; Arfaoui, I.; Cerullo, G.; Pileni, M.-P. Modulating Physical Properties of Isolated and Self-Assembled Nanocrystals Through Change in Nanocrystallinity. *Nano Lett.* **2013**, DOI: 10.1021/nl303898.
(28) Sun, Y.; Mayers, B.; Herricks, T.; Xia, Y. Polyol Synthesis of Uniform Silver Nanowires: A Plausible Growth Mechanism and the Supporting Evidence. *Nano Lett.* **2003**, *3*, 955−960.
(29) Wiley, B. J.; Im, S. H.; Li, Z.-Y.; McLellan, J.; Siekkinen, A.; Xia, Y. Maneuvering the Surface Plasmon Resonance of Silver Nanostructures Through Shape-Controlled Synthesis. *J. Phys. Chem. B* **2006**, *110*, 15666−15675.
(30) Huo, Z.; Tsung, C.-K.; Huang, W.; Zhang, X.; Yang, P. Sub-Two Nanometer Single Crystal Au Nanowires. *Nano Lett.* **2008**, *8*, 2041−2044.

(31) Lu, X.; Yavuz, M. S.; Tuan, H.-Y.; Korgel, B. A.; Xia, Y. Ultrathin Gold Nanowires Can Be Obtained by Reducing Polymeric Strands of Oleylamine-AuCl Complexes Formed via Aurophilic Interaction. *J. Am. Chem. Soc.* **2008**, *130*, 8900−8901.

(32) Park, H. S.; Cai, W.; Espinosa, H. D.; Huang, H. Mechanics of Crystalline Nanowires. *MRS Bull.* **2009**, *34*, 178−183.

(33) Jensen, L. L.; Jensen, L. Electrostatic Interaction Model for the Calculation of the Polarizability of Large Nobel Metal Nanostructures. *J. Phys. Chem. C* **2008**, *112*, 15697−15703.

(34) Jensen, L. L.; Jensen, L. Atomistic Electrodynamics Model for Optical Properties of Silver Nanoclusters. *J. Phys. Chem. B* **2009**, *113*, 15182−15190.

(35) Jensen, L.; Astrand, P.-O.; Mikkelsen, K. V. An atomic capacitance-polarizability model for the calculation of molecular dipole moments and polarizabilities. *Int. J. Quantum Chem.* **2001**, *84*, 513−522.

(36) Mayer, A. Formulation in terms of Normalized Propagators of A Charge-Dipole Model Enabling the Calculation of the Polarization Properties of Fullerenes and Carbon Nanotubes. *Phys. Rev. B* **2007**, *75*, 045407.

(37) Lammps. http://lammps.sandia.gov/ 2013.

(38) Foiles, S. M.; Baskes, M. I.; Daw, M. S. Embedded-Atom-Method Functions for the FCC Metals Cu, Ag, Au, Ni, Pd, Pt, and their Alloys. *Phys. Rev. B* **1986**, *33*, 7983−7991.

(39) Park, H. S.; Klein, P. A. Surface Cauchy-Born Analysis of Surface Stress Effects on Metallic Nanowires. *Phys. Rev. B* **2007**, *75*, 085408.

(40) Willets, K. A.; Duyne, R. P. V. Localized Surface Plasmon Resonance Spectroscopy and Sensing. *Annu. Rev. Phys. Chem.* **2007**, *58*, 267−297.

(41) Jacak, W. A. On Plasmon Polariton Propagation Along Metallic Nano-Chain. *Plasmonics* **2013**, 1−17.

(42) Scholl, J. A.; Koh, A. L.; Dionne, J. A. Quantum Plasmon Resonances of Individual Metallic Nanoparticles. *Nature* **2012**, *483*, 421−427.

(43) Liebsch, A. Surface-Plasmon Dispersion and Size Dependence of Mie Resonance: Silver Versus Simple Metals. *Phys. Rev. B* **1993**, *48*, 11317−11328.

(44) Link, S.; El-Sayed, M. A. Spectral Properties and Relaxation Dynamics of Surface Plasmon Electronic Oscillations in Gold and Silver Nanodots and Nanorods. *J. Phys. Chem. B* **1999**, *103*, 8410−8426.

(45) Meier, M.; Wokaun, A. Enhanced Fields on Large Metal Particles: Dynamic Depolarization. *Opt. Lett.* **1983**, *8*, 581−583.

(46) Ben, X.; Park, H. S. Size-Dependence of the Plasmon Ruler for Two-Dimensional Nanosphere Arrays. *J. Phys. Chem. C* **2011**, *115*, 15915−15926.

(47) McMahon, J. M.; Gray, S. K.; Schatz, G. C. Calculating Nonlocal Optical Properties of Structures with Arbitrary Shape. *Phys. Rev. B* **2010**, *82*, 035423.

(48) de Abajo, F. J. G. Nonlocal Effects in the Plasmons of Strongly Interacting Nanoparticles, Dimers, and Waveguides. *J. Phys. Chem. C* **2008**, *112*, 17983−17987.

(49) Ben, X.; Park, H. S. Size-Dependent Validity Bounds on the Universal Plasmon Ruler for Metal Nanostructure Dimers. *J. Phys. Chem. C* **2012**, *116*, 18944−18951.